Dalton Transactions

ROYAL SOCIETY OF CHEMISTRY

PAPER

View Article Online
View Journal | View Issue

Check for updates

Cite this: *Dalton Trans.*, 2025, **54**, 10140

Elucidation of the effects of *trans*/*cis*-isomerization of the cinnamate ligand on the structural, spectroscopic and magnetic properties of cobalt(II) single-molecule magnets†

Petr Halaš, [a] Ivan Nemec, [a] Erik Čižmár [b] and Radovan Herchel *[a]

Received 29th April 2025,
Accepted 22nd May 2025

DOI: 10.1039/d5dt01004g

rsc.li/dalton

Two new pseudo-octahedral Co(II) complexes **1** $[Co(neo)_2(trans\text{-}cin)]ClO_4$ and **2** $[Co(neo)_2(cis\text{-}cin)]ClO_4$ with *trans* and *cis*-cinnamic acid (Hcin) and neocuproine (neo) as ligands were prepared. Both complexes were characterized *via* single-crystal X-ray analysis, infrared spectroscopy, magnetic measurements, and EPR spectroscopy. DC magnetic susceptibility measurements revealed large axial magnetic anisotropy with axial zero-field splitting (ZFS) parameters D = 49.9 and 59.5 cm^{-1} and rhombicity E/D = 0.307 and 0.147 for **1** and **2**, respectively. These results were in accordance with CASSCF/NEVPT2 calculations. AC magnetic data showed the presence of slow relaxation of magnetization for both compounds in the applied DC field. UV irradiation studies in solution show that the complexes most likely undergo *trans*/*cis* photoisomerisation, which is, however, accompanied by side reactions and degradation. This was elucidated further utilizing DFT and TD-DFT calculations.

Introduction

Mononuclear single-molecule magnets (SMMs) represent a group of compounds exhibiting slow relaxation of magnetization on the level of single molecules, where only one metallic center is responsible for such behavior. In the past twenty years, progress has been made in improving the blocking temperature, with the more recent dysprosocenium derivative $[(Cp^{iPr5})Dy(Cp^*)][B(C_6F_5)_4]$ complex (Cp^{iPr5} = penta(isopropyl) cyclopentadienyl, Cp* = pentamethylcyclopentadienyl) reaching T_B = 80 K, thus surpassing liquid nitrogen temperature.[1]

One of the main drawbacks of the dysprosocenium complexes is their low stability in air, which has led many researchers to investigate transition metal complexes, mostly limited to Fe(II) and Co(II), to find more stable and easier to synthesize alternatives, albeit exhibiting lower blocking temperatures and barriers compared to Ln(III) SIMs. Polyhedron shapes such as trigonal prism[2] and deformed tetrahedron[3] seem to be the most promising to obtain a highly negative *D*-parameter with low rhombicity and thus axial type of magnetic anisotropy and low probability of the quantum tunnelling effect in Co(II) complexes. A prominent result was reported by Rechkemmer *et al.* for the $(HNEt_3)_2[Co(bmsab)_2]$ complex (bmsab = *N*,*N*′-1,2-phenylenebis(methanesulfonamide)).[4] This Co(II) based SIM possesses an axially elongated tetrahedral geometry and exhibits a U_{eff} value of over 200 cm^{-1} together with slow relaxation of magnetization in a zero applied static field while also being completely air- and moisture-stable.

Previous research has also shown that an axial type of anisotropy could be observed for octahedral Co(II) complexes with a positive *D*-parameter and high rhombicity, leading to slow relaxation of magnetization under the applied field.[5] It was concluded that increasing rhombicity causes the transition of the equatorial type of anisotropy into axial for positive *D* values. Another approach for synthesizing octahedral Co(II) SIMs was also published by Vallejo *et al.*, utilizing neocuproine and benzoic acid as ligands, which yield a deformed octahedral geometry possessing high anisotropy of the axial type.[6] Complexes of 3d metals are, therefore, still of much interest as they can provide much better stability and more facile synthetic procedures without the need for inert or anhydrous conditions.

For SMMs, spin state switching of the bulk samples is usually affected by the magnetic field; however, technological limitations arise when one tries to focus the magnetic field onto a scale of single molecules. Focus has, therefore, been given to pathways that affect spin state switching other than with the magnetic field, such as light irradiation. In the past,

[a]*Department of Inorganic Chemistry, Faculty of Science, Palacký University, 17. listopadu 12, 771 46 Olomouc, Czech Republic. E-mail: radovan.herchel@upol.cz*
[b]*Institute of Physics, Faculty of Science, P.J. Šafárik University, Park Angelinum 9, 04154 Košice, Slovakia*

†Electronic supplementary information (ESI) available. CCDC 2447436 and 2447437. For ESI and crystallographic data in CIF or other electronic format see DOI: https://doi.org/10.1039/d5dt01004g

many complexes containing azo-[7] or olefin[8] moieties, well known for their photoisomerization, have been prepared;[9] however, only limited research has been done on the influence of light-switchability on molecular magnetism.[10,11] Photoisomerisation of azo-compounds or olefins is usually limited to the liquid phase as crystal packing hinders the switching action; however, this obstacle may be overcome when working with single-molecule layers or polymeric films.[12] Additionally, problems with the reversibility of photoisomerisable compounds may arise due to degradation or side reactions taking place, such as [2 + 2] cycloaddition.[13]

We have previously reported on the synthesis and magnetochemical characterization of a new Co(II) complex containing neocuproine and *trans*-cinnamic acid as ligands and $[BPh_4]^-$ as the counterion, exhibiting slow relaxation of magnetization; however, no photoisomerisation could be observed in the solid phase.[14] As the *cis* isomer of cinnamic acid can be easily prepared by known methods utilizing UV irradiation,[15,16] we decided to explore and synthesize complexes with both isomers to compare their magnetochemical properties in order to evaluate their potential for future usage as light-switchable SIM-containing materials. Additionally, we chose to utilize a smaller perchlorate anion instead of tetraphenylborate to avoid difficulties with resolving solvent molecules trapped in cavities in the crystal structure.

We herein report on the synthesis and physicochemical characterization of two new Co(II) complexes **1** $[Co(neo)_2(trans\text{-}cin)]ClO_4$ and **2** $[Co(neo)_2(cis\text{-}cin)]ClO_4$ with *trans* and *cis*-cinnamic acid and neocuproine as ligands, together with a comparison of their magnetic properties studied by DC and AC magnetic susceptibility measurements, as well as EPR spectroscopy (Scheme 1). The aim of this work is to study the effects that *cis–trans* isomerism can have on both static and dynamic magnetic properties, such as zero-field splitting parameters or spin relaxation mechanisms.

Results and discussion

Synthesis

The *N*-butylammonium salt of *cis*-cinnamic acid was prepared according to a procedure published by Salum *et al.* utilizing a medium-pressure mercury lamp, providing the ligand in low to moderate yields.[16] The coupling constant obtained by ^1H NMR, together with a comparison of spectra with published ones, confirmed that the *cis* isomer has indeed been prepared (Fig. S1†).

Complexes were synthesized in a simple fashion by first mixing cobalt(II) perchlorate and neocuproine in a 1 : 2 ratio in acetone and subsequently adding an acetone solution of 1 equivalent of the corresponding cinnamate salt. Complex **1** formed big crystals over several days of slow evaporation, while complex **2** precipitated out of solution almost immediately and single crystals suitable for X-ray diffraction had to be grown in an extremely dilute solution (scale of 0.01 mmol in several ml of solvent). Products were then collected by filtration, washed with acetone, and dried in air. Polycrystalline products were then characterized by infrared spectroscopy (Fig. S2 and S3†) and elemental analysis.

To confirm phase purity, we performed X-ray powder diffraction (Fig. S4 and S5†). Compound **1** did not contain any noticeable impurities. However, compound **2** consistently contained small amounts of unknown impurities or phases even after repeated resyntheses. The elemental analysis confirmed sufficient purity of **2**, and we observed no impurities in magnetochemical studies.

Crystal structures

Both complexes crystallize in the $P2_1/n$ space group and possess 4 molecules per unit cell with Co(II) centres being hexacoordinate with the $\{N_4O_2\}$ chromophore (Fig. 1). Similarly to our previously published results,[14] the octahedral geometry is deformed due to steric hindrance provided by methyl groups of neocuproine and the small bite angle of donor oxygen atoms of cinnamate. Within crystal packing, π–π stacking interactions between the neocuproine rings are the only notable non-covalent contacts.

The cinnamate ligand is disordered in complex **1** with d(Co1–O1) = 2.077(4) Å, d(Co1–O2) = 2.319(4) Å and ∠(O1–Co1–O2) = 58.9(2)° for a fragment with an occupancy of 0.678 and d(Co1–O1) = 2.069(9) Å, d(Co1–O2) = 2.313(1) Å and ∠(O1–Co1–O2) = 58.1(4)° for a fragment with an occupancy of 0.322. Analysis using Shape 2.1 software confirmed that the poly-

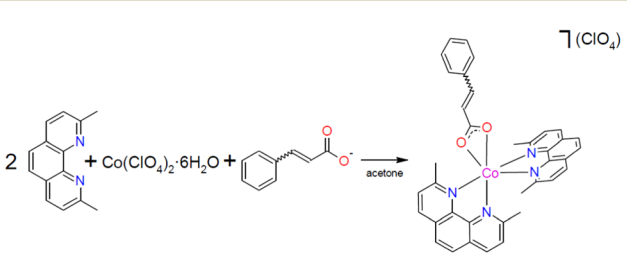

Scheme 1 Synthesis of compounds **1** and **2**.

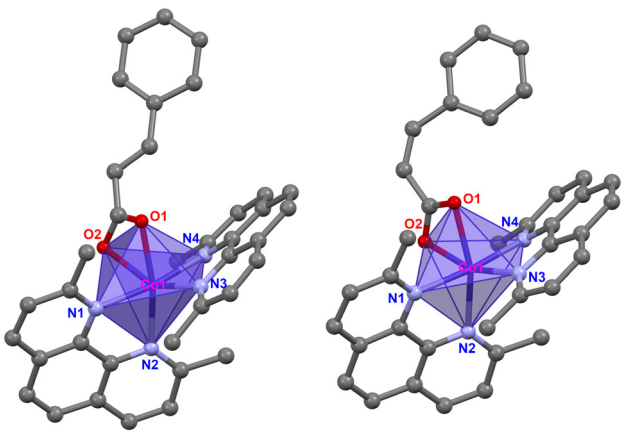

Fig. 1 Structure of complex cations of **1** (left) and **2** (right) with coordination spheres labeled. Hydrogen atoms were omitted for clarity.

hedron shape is indeed closest to the octahedral one, with continuous shape measure (CShM) values of 3.684 and 4.020 for the disordered fragments, respectively. A small cavity can be found using a 1.2 Å probe radius within the structure, occupying 0.3% of the unit cell volume.

In complex **2**, oxygen atoms are coordinated at nearly equal distances, with d(Co1–O1) = 2.182(1) Å, d(Co1–O2) = 2.153(1) Å and ∠(O1–Co1–O2) = 60.92(5)°. Similarly to complex **1**, the shape of the polyhedron is a deformed octahedron with a CShM value of 2.968. Again, small voids can be found within the structure, occupying 2.5% of the unit cell volume. The bond lengths and angles of the coordination polyhedra are summarized in Table S1.†

Static magnetic properties

The temperature dependence of magnetic moment at an inset field of B = 0.2 T and the field dependence of molar magnetization for both complexes at temperatures of T = 1.8, 5, 10, and 15 K are presented in Fig. 2. The measured effective magnetic moments at room temperature of $\mu_{\mathrm{eff}}/\mu_{\mathrm{B}}$ = 4.69 for complex **1** and $\mu_{\mathrm{eff}}/\mu_{\mathrm{B}}$ = 4.66 for complex **2** are much higher than the calculated spin-only value of $\mu_{\mathrm{eff}}/\mu_{\mathrm{B}} = g\sqrt{S(S+1)} = 3.87$ for the Co(II) system with S = 3/2 and g = 2.0, most likely due to the large unquenched orbital momentum. As shown in Fig. 2, $\mu_{\mathrm{eff}}/\mu_{\mathrm{B}}$ gradually decreases upon lowering the temperature down to 3.65 and 3.45 for **1** and **2**, respectively. Furthermore, isothermal molar magnetization at 1.8 K and 7 T reached $M_{\mathrm{mol}}/(N_{\mathrm{A}}\mu_{\mathrm{B}})$ = 2.14 and 2.06 for **1** and **2**, respectively, values much lower than the calculated $M_{\mathrm{mol}}/(N_{\mathrm{A}}\mu_{\mathrm{B}}) = g{\cdot}S = 3$.

This suggests that both complexes have large magnetic anisotropy and we therefore performed simultaneous fit of the aforementioned data with spin Hamiltonian (eqn (1)) comprising zero-field terms and the Zeeman term using POLYMAGNET software.[17]

$$\hat{H} = D(\hat{S}_z^2 - \hat{S}/3) + E(\hat{S}_x^2 - \hat{S}_y^2) + \mu_{\mathrm{B}}Bg\hat{S} \quad (1)$$

Parameters D and E represent axial and rhombic zero-field splitting parameters, respectively. The best fit for complex **1** was obtained with parameters D = 49.9 cm^{-1}, E/D = 0.307, g_{xy} = 2.470 with g_z fixed at 2.0 and temperature-independent paramagnetism of $\chi_{\mathrm{TIP}} = 8.0 \times 10^{-9}$ m^3 mol^{-1}.

For complex **2**, the best fit was achieved with parameters D = 59.5 cm^{-1}, E/D = 0.147, g_{xy} = 2.347 with g_z fixed at 2.0 and temperature-independent paramagnetism of $\chi_{\mathrm{TIP}} = 15.1 \times 10^{-9}$ m^3 mol^{-1}. It should be noted that analogous analysis was attempted with negative D-values and zero and non-zero rhombicity for both complexes, but without reaching a better agreement with the experimental data.

Dynamic magnetic properties

To investigate the presence of slow relaxation of magnetization, AC susceptibility measurements were performed for both complexes. First, AC susceptibility was measured at a fixed temperature of 2 K with varying static magnetic fields. Data were fitted utilizing the SciPy module for Python.[18]

Field-dependence of AC susceptibility could be analyzed in the field range of 0.05 to 1 T for complex **1** (Fig. 3). No out-of-

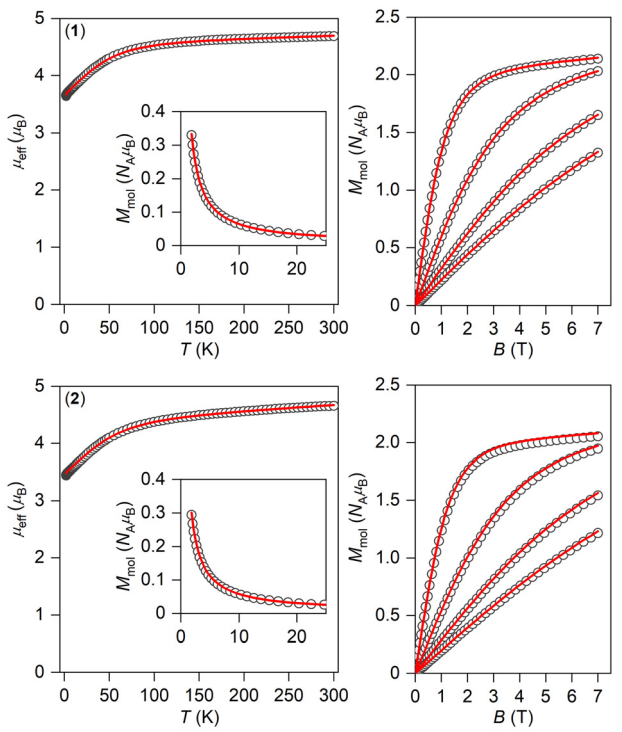

Fig. 2 Temperature dependence of magnetic moment and isothermal field dependence of molar magnetization of **1** (top) and **2** (bottom). Empty symbols – experimental data, full red lines – calculated data.

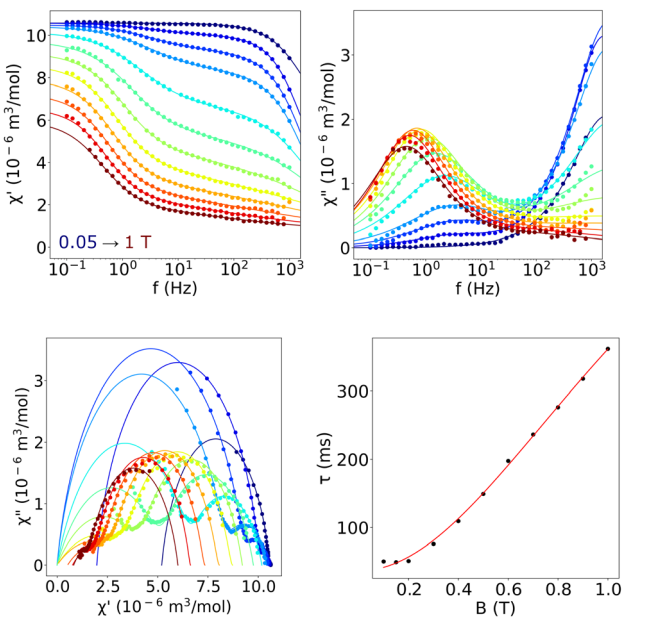

Fig. 3 Field-dependent AC susceptibility data of **1**. Top – real (left) and imaginary (right) parts of susceptibility *vs.* frequency. Lines represent the best fit into the Debye model. Bottom – Argand diagram (left) and best fit of relaxation times (right).

phase susceptibility was observed at zero DC field. We observed the appearance of a high frequency relaxation channel at lower fields and an additional low frequency relaxation channel at higher fields. Experimental data were fitted into a one-component or two-component Debye model for fields above 0.05 T, according to eqn (2).

$$\chi(2\pi f) = \chi_S + \sum_{n=1} \frac{\chi_{T_n} - \chi_{T_{n-1}}}{1 + (i2\pi f \tau_n)^{1-\alpha_n}} \quad (2)$$

The fitted parameters are summarized in the ESI (Table S3†). Attempts were made to fit the obtained relaxation times simultaneously with temperature-dependent ones. However, no decent fit was obtained; therefore, both datasets were analyzed separately. Low frequency channel relaxation times were fitted using the following eqn (3), composed of quantum tunneling (QTM) (b_1, b_2) and phonon bottleneck (PB) (G) terms.

$$\frac{1}{\tau} = \frac{b_1}{1 + b_2 B^2} + GT^2 \quad (3)$$

The best fitted parameters were b_1 = 26.2(2.3) s^{-1}, b_2 = 15.0 (1.9) T^{-2} and G = 0.22(0.01) K^{-2} s^{-1}. It should be noted that a similar but slightly worse fit was obtained with QTM and direct terms. This is in accordance with the used QTM + PB model as PB is just a hindered direct process.[19] The high-frequency relaxation channel was not analyzed further due to large uncertainty, especially at high fields, of the obtained relaxation times.

Next, the temperature dependence of AC magnetic susceptibility was analyzed in the range of 1.9 to 2.8 K. At higher temperatures, the out-of-phase susceptibility diminished too much to provide any reliable fits. The static field was set to 0.5 T. Data were measured up to 997 Hz; however, this was not enough to properly describe the high-frequency relaxation channel, which again resulted in deviations of relaxation times being higher than fitted values. We, therefore, decided to fit only the low-frequency relaxation channel up to 18 Hz into the one-component Debye model (Fig. 4 and Table S4†). The obtained relaxation times were fitted into eqn (4) comprising the Raman (C) term. It should be noted that attempts were made to fit data into models containing the Orbach term; however, the obtained values of barrier energy were not in accordance with DC magnetic measurements (Fig. S6†).

$$\frac{1}{\tau} = CT^n \quad (4)$$

The obtained parameters were C = 1.19(0.08) s^{-1} K^{-n} and n = 2.56(0.09). As the coefficient n is much closer in value to 2 rather than to the expected range of 5 to 9 for Kramers doublets, we suspect that it is indeed the aforementioned phonon bottleneck process.

Similarly, for complex **2**, increasing the magnetic field also leads to the increase in out-of-phase AC susceptibility and the consequent appearance of a second relaxation process at higher fields, as can be seen in Fig. 5. Thus, data were fitted into a one-component Debye model and, for fields above 0.15 T, into a two-component Debye model according to eqn (2). Maximal out-of-phase susceptibility was obtained at 0.15 T. Therefore, subsequent temperature-dependent data were measured at a fixed DC field of 0.15 T in the range of 1.9 to 5 K and fitted into a one-component Debye model. The fitted parameters are reported in the ESI – Tables S5 and S6.† The low-frequency channel was analyzed separately and fitted into a model comprising QTM (Fig. S7†). The obtained relaxation times from field- and temperature-dependent data of the high-frequency process were then fitted simultaneously with eqn (5), containing direct (A) and Raman (C, n) relaxation process terms (Fig. 5). The exponent value m was set to 4, as Co(II) is a Kramers ion.

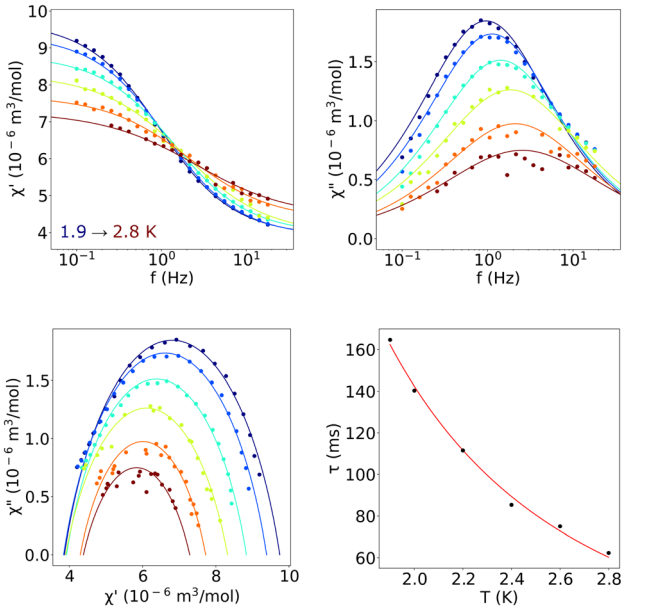

Fig. 4 Temperature-dependent AC susceptibility data of **1**. Top – real (left) and imaginary (right) parts of susceptibility *vs.* frequency. Lines represent the best fit into the Debye model. Bottom – Argand diagram (left) and best fit of relaxation times (right).

$$\frac{1}{\tau} = CT^n + ATB^m \quad (5)$$

This yielded parameters C = 173(9) s^{-1} K^{-n}, n = 2.15(0.07) and A = 14 552(1107) s^{-1} K^{-1} T^{-4}. As n is again much lower than the expected values of 5 to 9, we suspect that the Raman relaxation mechanism is rather a phonon bottleneck effect. Attempts were again made to fit the data into models containing the Orbach term; however, the obtained barrier values were not in accordance with DC magnetic measurements (Fig. S8†).

EPR spectroscopy

The X-band EPR spectra of compounds **1** and **2** were recorded in the temperature range from 2 K to 70 K. A typical decrease in the signal intensity and line broadening with increasing temperature was observed as expected for a large zero-field splitting between the lowest Kramers doublets (Fig. S9†). Thus,

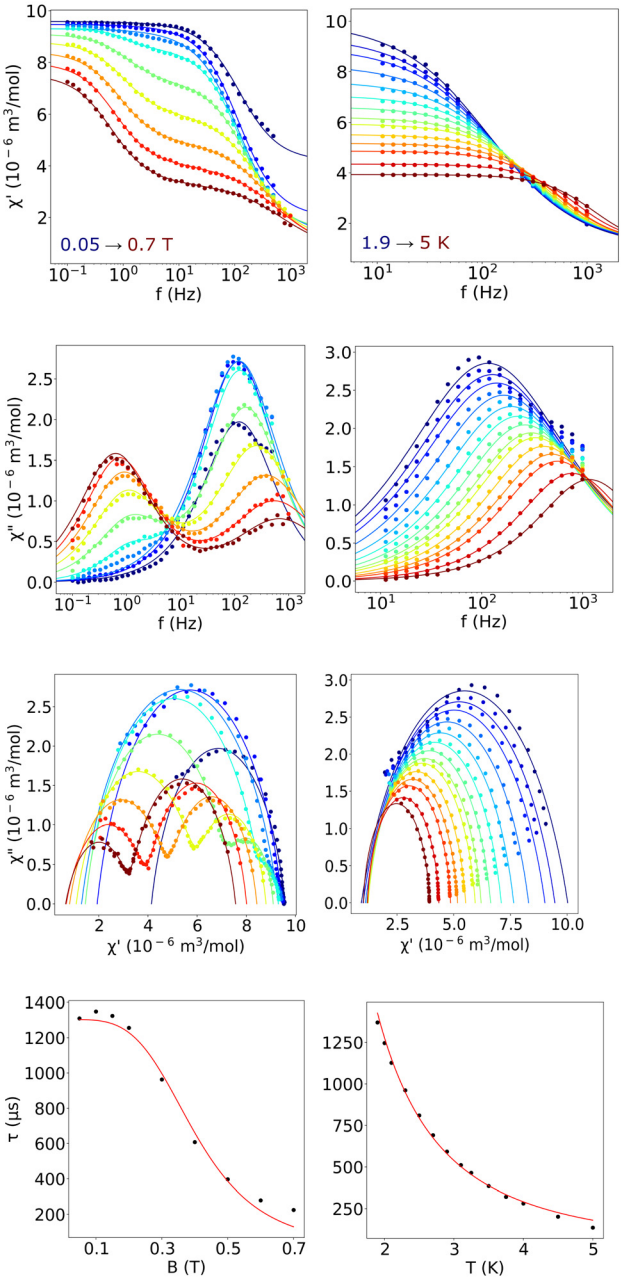

Fig. 5 Field-dependent (left) and temperature-dependent (right) AC susceptibility of **2**. Real (1st row) and imaginary (2nd row) parts of susceptibility *vs.* frequency. Lines represent the best fit into the Debye model. Argand diagrams (3rd row) and best simultaneous fit of relaxation times (4th row).

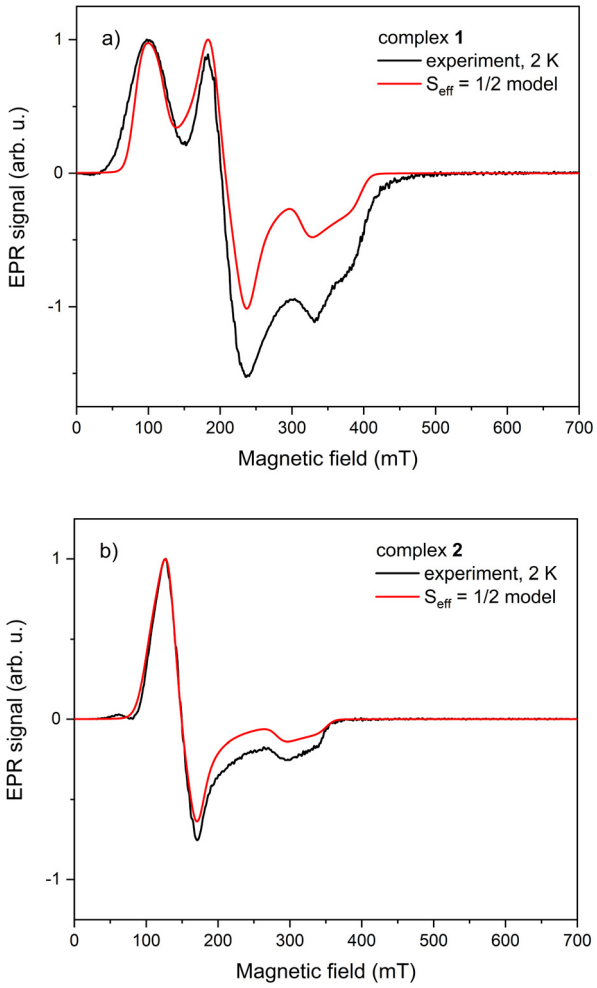

Fig. 6 The X-band EPR data (black solid lines) of complexes **1** (a) and **2** (b) obtained at 2 K, including the simulations using the effective spin S_{eff} = 1/2 model (solid red lines) with parameters summarised in Table 1.

a simplified effective spin S_{eff} = 1/2 model describing only the ground Kramers doublet for the analysis of EPR at low temperatures can be applied. The mixing of higher excited states with the ground Kramers doublet as a consequence of the spin–orbit coupling then yields highly anisotropic effective *g*-factors. The simulation of EPR spectra shown in Fig. 6 was performed within the EasySpin simulation package.[20] The hyperfine interaction A' with nuclear spins was not clearly resolved for all *g*-factor components, but its effect is clear for the lowest *g*-factors (or the highest resonance field part of the spectra). To fully describe the experimental spectra, hyperfine interaction A' and an anisotropic convolutional broadening ΔB (full-width at half-height) were included in the simulation. The obtained parameter set is summarised in Table 1. Possible disorder in **1** yielding two different sets of the parameters was not distinguished in the experimental EPR spectra, possibly due to their small variation. When applying the Griffith–Figgis formalism[21] to obtain the effective *g*-factors of the ground Kramers doublet, it seems that both positive and negative axial field parameters $|\Delta_{ax}| \approx 1050$ cm^{-1} seem to be in line with expected values if a substantial rhombic $\Delta_{rh}/\Delta_{ax} \approx 1/3$ parameter is included for **1**. This confirms the critical role of the rhombic term in the description of the magnetic properties of **1**. In the case of **2**, the only compatible combination of Δ_{rh} and Δ_{ax} seems to be when $\Delta_{ax} \approx 1050$ cm^{-1} and the ratio of $\Delta_{rh}/\Delta_{ax} \approx 0.104$. The prediction of the effective *g*-factors for both complexes is shown in Fig. S10 and S11.† The results are

Table 1 Parameters of the effective spin S_{eff} = 1/2 model and spin Hamiltonian formalism estimated for the analysis of the X-band EPR for complexes **1** and **2**

Complex, approach	Parameters
1, S_{eff} = 1/2 model, estimated from data	$[g'_1, g'_2, g'_3]$ = [1.89, 3.17, 6.57] $[A'_1, A'_2, A'_3]$ = [275, 275, 470] MHz $[\Delta B_1, \Delta B_2, \Delta B_3]$ = [22, 38, 75] mT
1, S_{eff} = 1/2 model, *x*,*y*,*z* assignment	$[g'_x, g'_y, g'_z]$ = [3.17, 6.57, 1.89] $[A'_x, A'_y, A'_z]$ = [275, 470, 275] MHz
1, spin Hamiltonian, *x*,*y*,*z* assignment	$[g_x, g_y, g_z]$ = [2.49, 2.55, 2.22] $[A_x, A_y, A_z]$ = [216, 182, 323] MHz E/D = 0.235
2, S_{eff} = 1/2 model, estimated from data	$[g'_1, g'_2, g'_3]$ = [2.12, 4.47, 5.55] $[A'_1, A'_2, A'_3]$ = [255, 310, 400] MHz $[\Delta B_1, \Delta B_2, \Delta B_3]$ = [22, 38, 75] mT
2, S_{eff} = 1/2 model, *x*,*y*,*z* assignment	$[g'_x, g'_y, g'_z]$ = [4.47, 5.55, 2.12] $[A'_x, A'_y, A'_z]$ = [310, 400, 255] MHz
2, spin Hamiltonian, *x*,*y*,*z* assignment	$[g_x, g_y, g_z]$ = [2.54, 2.50, 2.16] $[A_x, A_y, A_z]$ = [176, 180, 260] MHz E/D = 0.078

consistent with the predicted positive D parameter from CASSCF/NEVPT2 calculations for **2**. On the other hand, only judging from EPR analysis, the sign of D for **1** cannot be unambiguously identified. But taking into account the results of the magnetic data analysis and CAS(11e, 12o) CASSCF/NEVPT2 calculations, both complexes can be considered with $D > 0$. In such a case, one can assign g'_x, g'_y, g'_y and later to real g_x, g_y, g_z of the spin Hamiltonian formalism using an approach outlined in ref. 22. Using all possible combinations of g'_1, g'_2, g'_3 and the average g-factor obtained from the experimental room-temperature value of the effective magnetic moment, one obtains the E/D ratio and a unique assignment of *x*,*y*,*z*-components of the g-factors and anisotropic hyperfine interaction A. Unfortunately, the values of D and E cannot be directly estimated from such analysis of X-band EPR spectra. The results of this procedure summarised also in Table 1 are in good agreement with the analysis of the magnetic data. The obtained E/D values of 0.235 and 0.078 for **1** and **2**, respectively, seem to be slightly underestimated. This is potentially affected by the accuracy in the estimation of the diamagnetic and temperature-independent paramagnetic contribution of the system to obtain the average g-factor from the room-temperature value of the magnetic moment required for the analysis.

Theoretical calculations

Geometry optimization and ZFS parameters were obtained using ORCA 5.0.4 software.[23,24] Complex cations were extracted from crystal structures and positions of hydrogens were first optimized using the DFT method utilizing the BP86 functional.[25] Ahlrichs' def2-TZVP basis set was chosen for all atoms except for hydrogen and carbon, where a less demanding def2-SVP basis set was chosen.[26] The resolution of identity (RI) approximation[27] together with the def2/J auxiliary basis set[28] was employed. To obtain ZFS parameters, the post-Hartree–Fock method CASSCF(7e, 5o)[29] with NEVPT2 correction[30,31] was used. The same basis sets were used with the addition of def2-TZVP/C for correlation fitting[32] and chain-of-sphere approximation[33] (RIJCOSX) was turned on. The obtained ZFS parameters are summarized in Table 2 for the active space defined by five metal 3d-orbitals, CAS(7e, 5o), and also for the larger active space defined by two additional ligand base bonding orbitals and extra five 4d-orbitals, CAS (11e, 12o) – Fig. S12.†

Due to the presence of disorder, both complex species of **1** were analyzed separately (labeled as **1_a** and **1_b**). The calculated splitting of d-orbitals for **1** and **2** resembles the pattern typical of a pseudo-octahedral coordination geometry, set of t_{2g} and e_g orbitals, and e_2 orbitals are more split for **1** than for **2** (Fig. 7a). Due to lower symmetry, the $^4T_{1g}$ ligand-field term (in ideal O_h symmetry) is split into three terms within *ca.* 1600 cm^{-1} (Fig. 7b). Finally, spin states for S = 3/2 are split into two Kramers states separated by *ca.* 120–128 cm^{-1} for **1** and by 108 cm^{-1} for **2**. Other excited Kramers states are located at much higher energies, and thus, the spin Hamiltonian formalism is valid. Both complexes possess large magnetic anisotropy and non-zero rhombicity. This is in good agreement with the fitted values from DC magnetic measurements. Complexes may possess both easy-axis and easy-plane type of anisotropy due to high rhombicity;[34] we therefore analyzed the ground state Kramers doublet (S_{eff} = 1/2), which resulted in g_1, $g_2 < g_{avg}$ and $g_{avg} < g_3$ and we can thus conclude that both complexes possess the axial type of magnetic anisotropy. This is also demonstrated in Fig. S13,† in which the

Table 2 Comparison of zero-field splitting parameters obtained from theoretical calculations and experimental data analysis

Compound	**1**	**2**
Fitted parameters from experimental DC data		
D (cm^{-1})	49.9	59.5
E/D	0.307	0.147
g_{xy}	2.470	2.347
g_z (fixed)	2.0	2.0
CASSCF/NEVPT2 results with CAS(7e, 5o)		
D (cm^{-1})	54.1/−57.0	53.7
E/D	0.328/0.330	0.121
g_x	2.353/2.342	2.458
g_y	2.752/2.020	2.625
g_z	2.031/2.777	2.035
g_{iso}	2.379/2.380	2.372
Kramers doublets with an effective spin of S_{eff} = 1/2		
g_1	1.593/1.572	2.057
g_2	2.381/2.327	3.983
g_3	7.428/7.513	6.052
g_{avg}	3.800/3.804	4.031
CASSCF/NEVPT2 results with CAS(11e, 12o)		
D (cm^{-1})	52.6/55.4	53.0
E/D	0.326/0.331	0.116
g_x	2.354/2.343	2.461
g_y	2.753/2.777	2.629
g_z	2.027/2.016	2.031
g_{iso}	2.378/2.379	2.374
Kramers doublets with an effective spin of S_{eff} = 1/2		
g_1	1.606/1.595	2.073
g_2	2.396/2.363	4.031
g_3	7.416/7.486	6.018
g_{avg}	3.806/3.815	4.041

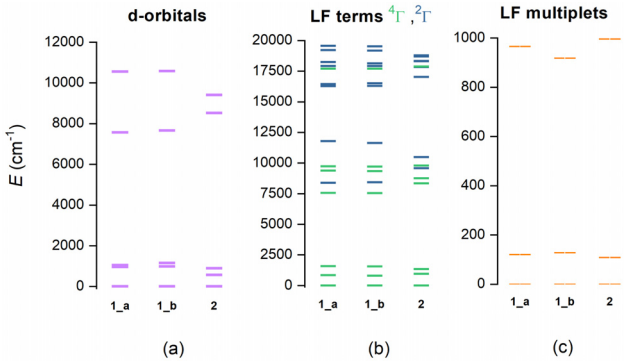

Fig. 7 Results of the CASSCF/NEVPT2 calculations for **1** and **2**: (a) the plot of the d orbital splitting calculated using the *ab initio* ligand field theory (AILFT) using CAS(7e, 5o), (b) low-lying ligand-field terms (LFT) and (c) ligand-field multiplets (LFM) resulting from CAS(11e, 12o). Note: different multiplicities of LFT are shown in different colors.

respective *D*-tensors and three-dimensional magnetization data overlaid over respective molecular structures are depicted. Moreover, this finding is also in good agreement with AC magnetic measurements, as the axial type of magnetic anisotropy is needed for the observed slow relaxation of magnetization. Additional analysis with the SINGLE_ANISO module also showed a large predisposition to quantum tunnelling between ground states with opposite magnetization with matrix elements of the transversal magnetic moment being equal to 0.666/0.659 and 1.02 for complexes **1** and **2**, respectively (Fig. S13†). We presume that this is the major contributing factor to why no slow relaxation was observed in the zero DC field.

Irradiation studies

In order to determine if our complexes undergo photoisomerisation, we investigated the effect of UV irradiation utilizing UV/Vis spectroscopy. Methanol solutions of complexes (10 μM) were subjected to irradiation using a 254 nm UV lamp (9 W) for 10-minute intervals between measurements.

For complex **1** (Fig. 8 – top), we can see a gradual decrease in absorbance, as should be expected in the case of the formation of the *cis* isomer; however, more irradiation causes a continual drop below the absorbance level of pure *cis*-isomeric complex **2**. We therefore suspect that isomerization is accompanied by other side-reactions, most likely [2 + 2] cycloaddition.

This was confirmed when we performed the same experiment for complex **2** (Fig. 8 – bottom), where a first increase of absorbance could be observed due to the formation of the *trans* isomer. When equilibrium was reached, more irradiation only led to unwanted side reactions as is evident from the continual drop of absorbance even below the level before irradiation. Interestingly, the band around 200 nm increases with prolonged irradiation in contrast to complex **1**. It is possible that different side products are formed for both complexes.

A sudden drop or rise of the 270 nm band can be observed for **1** and **2**, respectively, while the 230 nm band absorbance

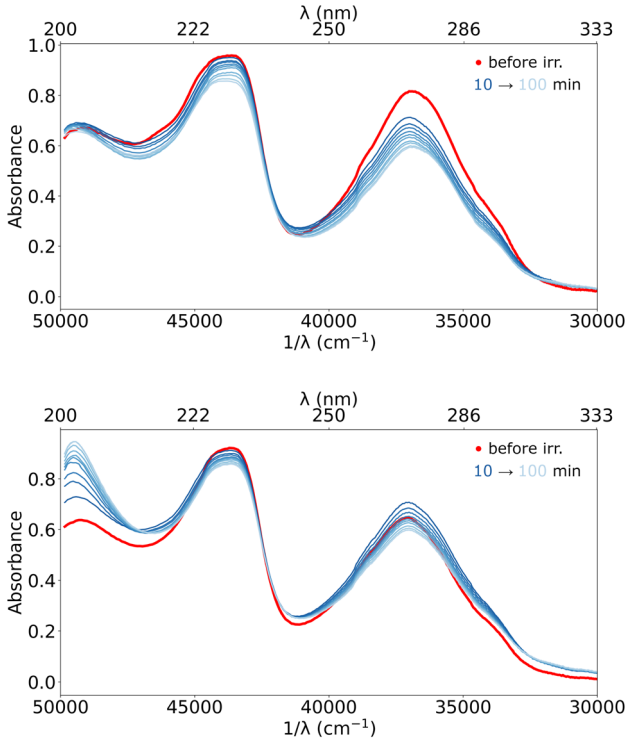

Fig. 8 UV/Vis spectrum of complexes **1** (top) and **2** (bottom) before and after irradiation with a 254 nm lamp.

drops only slightly for both compounds after the first 10 minutes of irradiation. Any further irradiation leads to a slow decrease of both bands, which supports our hypothesis that photoequilibrium of both isomers is achieved within the first 10 minutes of irradiation, and further irradiation leads to degradation. Unfortunately, the isomers cannot be selectively switched by different wavelengths as their absorbance maxima are nearly identical and differ only in extinction coefficients.

The same experiment was performed for deprotonated forms of both isomers of cinnamic acid, where a similar trend was observed (Fig. S14†). We, therefore, conclude that our complexes undergo photoisomerization, which is, however, accompanied by side reactions that lead to the degradation of the complexes.

Additionally, DFT/TD-DFT calculations were done using ORCA 6.0[35] in order to calculate UV-VIS spectra of both *trans*/*cis* isomers of cinnamate, their complexes **1** and **2**, and also possible products of photodimerization of *trans*-cinnamate, namely, dianions of α-truxillic acid and β-truxinic acid. First, the molecular geometries were optimized with the range hybrid CAM-B3LYP functional[36] with D4 dispersion correction[37] using the C-PCM solvation model for methanol.[38,39] Next, TD-DFT calculations were performed with the same functional, and the respective UV-VIS spectra are shown in Fig. 9. The calculated dominant bands of cinnamates located within 38–40 000 cm^{-1} are shifted to higher energies for *cis*-cinnamate (band maximum located at 39 757 cm^{-1}) in comparison with *trans*-cinnamate (band maximum located at 38 423 cm^{-1}).

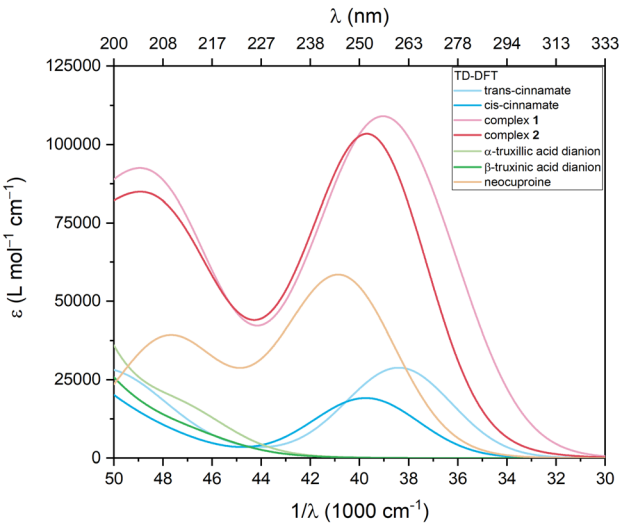

Fig. 9 UV-VIS spectra calculated by TD-DFT on optimized molecular geometries using the PBE0 hybrid functional.

With the help of Natural Transition Orbitals (NTOs), these transitions were assigned to π → π* transitions involving the double bond of cinnamate (Fig. S15 and S16†). The TD-DFT results of Co(II) complexes **1** and **2** showed that the band maxima are located at 39 049 cm^{-1} for **1** and at 39 709 cm^{-1} for **2** (Fig. 9). These bands have two main contributions as deduced from the respective NTOs: the first one located at lower energies comes from π → π* transitions of the cinnamate ligand, and the second one comes from π → π* and LMCT transitions of neocuproine ligands (Fig. S17 and S18†). This is in accordance with the spectrum calculated for free neocuproine (Fig. 9). It is worth mentioning that dianions of α-truxillic acid and β-truxinic acid, possible outcomes of photoreactions, should absorb light at much higher energy.

Moreover, the theoretical evolution of the UV-VIS spectra following the *trans* ↔ *cis* isomerization of the cinnamate anion and the Co(II) complex $[Co(neo)_2(cin)]^+$ was calculated as depicted in Fig. 10. It suggests that the main band at 38–40 000 cm^{-1} should lose the intensity and shift to higher energies during the *trans* → *cis* reaction and these changes are much more pronounced in the free cinnamate anion than in the respective Co(II) complex. This agrees with the experimental observation for **1** (Fig. 8, top) and *trans*-cinnamate (Fig. 8, top), and for short-term (ca up to 10 minutes) photoirradiation experiments for **2** (Fig. 8, bottom) and *cis*-cinnamate (Fig. 8, bottom). This suggests that the production of photodegradation side-products is enhanced in **2**.

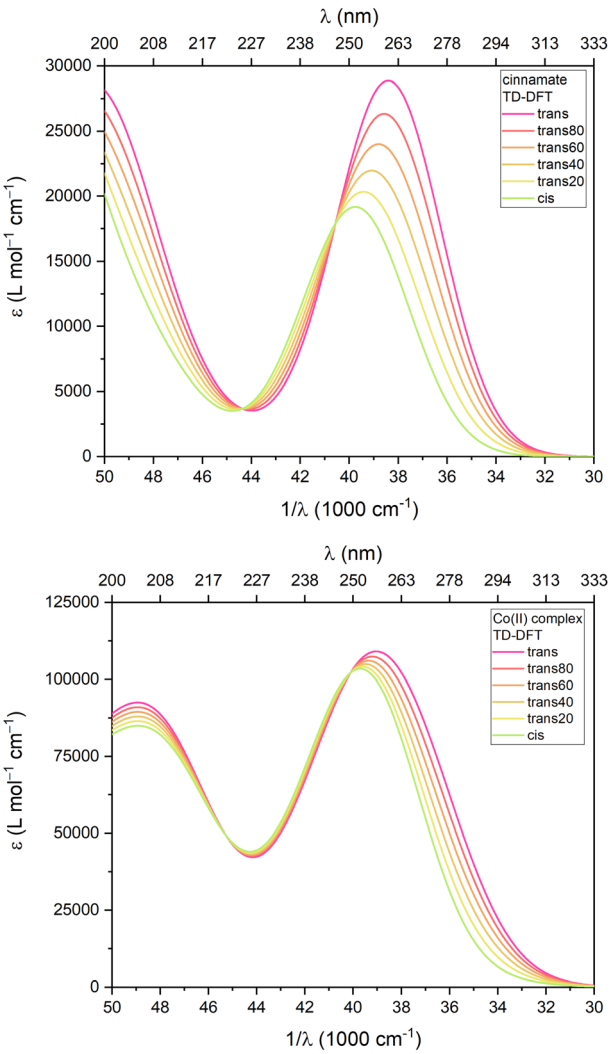

Fig. 10 UV-VIS spectra calculated by TD-DFT on optimized molecular geometries using the PBE0 hybrid functional showing *trans*–*cis* isomerization for the cinnamate anion (top) and for the Co(II) complex (bottom).

Experimental

Preparation of *n*-butylammonium *cis*-cinnamate

1 mmol of *trans*-cinnamic acid was dissolved in 100 ml of acetonitrile in a 250 ml quartz Erlenmeyer flask. To this, 1.1 mmol of *n*-butylamine was added and the mixture was subjected to UV irradiation with a medium-pressure mercury lamp for 4 hours under constant stirring (**CAUTION**: care must be taken to protect eyes and skin from intense UV radiation; protective gear and glasses should be used during irradiation; working in a fume hood is advisable as the lamp produces ozone). The mixture was then cooled in a fridge to complete the crystallization. The solid product was filtered off under reduced pressure and dried in air. Yield: 106 mg (48%). Purity was confirmed by ^1H NMR, which was in accordance with the published spectrum[16] with the coupling constant $^3J_{HH}$ between C=C hydrogens of 12.7 Hz, typical of the *cis* isomer of cinnamic acid (Fig. S1†).

Synthesis of complex 1

36.6 mg (0.1 mmol) of $Co(ClO_4)_2{\cdot}6H_2O$ was dissolved in 5 ml of acetone together with 43.4 mg (0.2 mmol) of neocuproine hemihydrate. To this was added a solution of 14.8 mg

(0.1 mmol) of *trans*-cinnamic acid with 13.8 μl (0.1 mmol) of triethylamine in 5 ml of acetone under stirring. A pink solid product was obtained by reducing the volume to 3 ml by blowing nitrogen gas and stirring overnight. Red crystals were filtered off, washed with a small amount of cold acetone, and dried in air. Red block single crystals of X-ray diffraction quality were obtained by undisturbed slow evaporation of the solvent. Yield: 44 mg (61%). FT-IR (cm^{-1}): 3062(w), 3021(w), 1708(w), 1631(w), 1590(m), 1564(w), 1541(w), 1496(s), 1451(m), 1421(m), 1359(m), 1294(w), 1246(w), 1224(w), 1153(w), 1073 (vs), 979(m), 860(s), 815(w), 778(m), 731(m), 718(w), 693(w), 681(w), 655(w), 621(m), 584(w), 551(w), 435(w). Anal. calcd for $C_{37}H_{31}ClCoN_4O_6$: C, 61.6; H, 4.3; N, 7.8. Found: C, 60.9; H, 4.3; N, 7.8.

Synthesis of complex 2

36.6 mg (0.1 mmol) of $Co(ClO_4)_2{\cdot}6H_2O$ was dissolved in 5 ml of acetone together with 43.4 mg (0.2 mmol) of neocuproine hemihydrate. To this was added a solution of 22.1 mg (0.1 mmol) of *n*-butylammonium *cis*-cinnamate in 5 ml of acetone with a few drops of water to dissolve the salt under stirring. Complex **2** precipitated within minutes after the addition of the *cis*-cinnamate salt and was left stirring overnight. Pink microcrystals were filtered off, washed with acetone, and dried in air. Pink single crystals suitable for X-ray diffraction analysis were prepared using 0.1 molar equivalents of reactants with the same volume of solvent and leaving the solution undisturbed in a fridge overnight. Yield: 63 mg (87%). FT-IR (cm^{-1}): 3066(w), 3019(w), 1705(w), 1626(w), 1591(m), 1563(w), 1533(m), 1496(s), 1465(m), 1436(s), 1361(s), 1327(w), 1294(w), 1224(w), 1153(w), 1084(vs), 1034(m), 859(s), 848(m), 810(w), 772(w), 731(w), 701(w), 655(w), 621(m), 550(w). Anal. calcd for $C_{37}H_{31}ClCoN_4O_6$: C, 61.6; H, 4.3; N, 7.8. Found: C, 61.2; H, 4.3; N, 7.7.

Instrumentation

Elemental analysis (C, H, N) was performed on a Thermo Scientific Flash 2000 analyzer. Infrared spectra were recorded on a JASCO FT/IR-4700 spectrometer utilizing the ATR technique. UV-VIS spectra were recorded on a GBC Scientific Instruments Cintra 3030. X-ray powder diffraction was recorded on a Rigaku MiniFlex 600. NMR spectra were recorded on a Varian 400 MHz NMR spectrometer. DC magnetic measurements were done on a Quantum Design MPMS3. AC magnetic measurements were done on a Quantum Design MPMS-XL. EPR spectra were recorded on a Bruker ELEXSYS II E500.

Crystallography

The X-ray diffraction data for orange crystals of **1** and **2** were collected using an XtaLAB Synergy-I diffractometer equipped with a HyPix3000 hybrid pixel array detector and a microfocused PhotonJet-I X-ray source (Cu Kα, 1.54184 Å). Absorption corrections were applied using the program CrysAlisPro 1.171.40.82a.[40] The crystal structures were solved using the SHELXT program[41] and refined using the full matrix least-squares procedure with SHELXL[42] in OLEX2 (version 1.5).[43] All non-hydrogen atoms were refined anisotropically, while hydrogen atoms were located from the Fourier difference map and refined using the "riding" model with $U_{iso}(H) = 1.2(-CH_2)$ or $1.5(-CH_3)U_{eq}$. Powder diffraction data were collected using a MiniFlex600 (Rigaku) equipped with the Bragg–Brentano geometry and with iron-filtered $CuK_{a1,2}$ radiation.

Non-routine aspects of refinement. In **1**, the cinnamate ligand is disordered over two positions, with the ratio of site occupation factors being 0.634 : 0.322. To build the model of disorder, it was necessary to use an extensive set of SHELXL restraints (SIMU, SADI) and constraints (EADP).

Conclusions

The incorporation of *trans*/*cis*-isomers of cinnamic acid resulted in two Co(II) complexes, **1** and **2**, in which the carboxylic moiety is coordinated in a bidentate fashion. However, the respective Co–O bond distances are very uneven in **1** in contrast to **2**, resulting in a shape closer to the ideal octahedron for **2**. These distinctions in the ligand fields are reflected in different sizes of ZFS parameters, *D* and *E*, deduced from the analysis of DC magnetic data. The easy-axis type of magnetic anisotropy for both complexes was further confirmed experimentally with X-band EPR and theoretically with CASSCF/NEVPT2 calculations. Although both complexes underwent photoisomerization in the solution, longer exposure to light resulted in side-reactions and degradations. To conclude, herein we provided evidence that different geometric isomers of the ligand alter both static and dynamic magnetic properties of these field-induced photoswitchable SMMs; however, their low photostability urges for other suitable molecular systems.

Author contributions

Petr Halaš: formal analysis, investigation, software, visualization, and writing – original draft. Ivan Nemec: formal analysis and investigation. Erik Čižmár: formal analysis, investigation, and visualization. Radovan Herchel: conceptualization, formal analysis, software, visualization, and writing – review & editing.

Data availability

The data supporting this article have been included as part of the ESI.† Crystallographic data for compounds **1** and **2** have been deposited at the CCDC under deposition numbers 2447436 and 2447437.†

Conflicts of interest

There are no conflicts to declare.

Acknowledgements

This research was funded by Palacký University in Olomouc projects IGA_PrF_2024_009 and IGA_PrF_2023_007. This work was also supported by the Slovak Research and Development Agency under Contracts APVV-20-0512, APVV-22-0172, and APVV-23-0006.

References

1 F. S. Guo, B. M. Day, Y. C. Chen, M. L. Tong, A. Mansikkamäki and R. A. Layfield, *Science*, 2018, **362**(6421), 1400–1403.
2 B. Yao, M. K. Singh, Y. F. Deng, Y. N. Wang, K. R. Dunbar and Y. Z. Zhang, *Inorg. Chem.*, 2020, **59**(12), 8505–8513.
3 S. Sottini, G. Poneti, S. Ciattini, N. Levesanos, E. Ferentinos, J. Krzystek, L. Sorace and P. Kyritsis, *Inorg. Chem.*, 2016, **55**(19), 9537–9548.
4 Y. Rechkemmer, F. D. Breitgoff, M. Van Der Meer, M. Atanasov, M. Hakl, M. Orlita, P. Neugebauer, F. Neese, B. Sarkar and J. Van Slageren, *Nat. Commun.*, 2016, **7**(1), 10467.
5 R. Herchel, L. Váhovská, I. Potočňák and Z. Travnicek, *Inorg. Chem.*, 2014, **53**(12), 5896–5898.
6 J. Vallejo, M. Viciano-Chumillas, F. Lloret, M. Julve, I. Castro, J. Krzystek, M. Ozerov, D. Armentano, G. De Munno and J. Cano, *Inorg. Chem.*, 2019, **58**(23), 15726–15740.
7 S. Kume, M. Kurihara and H. Nishihara, *Chem. Commun.*, 2001, (17), 1656–1657.
8 L. Chen, Y. Tan, H. Xu, K. Wang, Z. H. Chen, N. Zheng, Y. Q. Li and L. R. Lin, *Dalton Trans.*, 2020, **49**(46), 16745–16761.
9 V. Guerchais and H. Le Bozec, *Molecular organometallic materials for optics*, 2010, pp. 171–225.
10 K. Rogacz, M. Brzozowska, S. Baś, K. Kurpiewska and D. Pinkowicz, *Inorg. Chem.*, 2022, **61**(41), 16295–16306.
11 K. Rogacz, M. Magott, S. Baś, M. Foltyn, M. Rams and D. Pinkowicz, *RSC Adv.*, 2024, **14**(21), 14515–14522.
12 L. R. Lin, X. Wang, G. N. Wei, H. H. Tang, H. Zhang and L. H. Ma, *Dalton Trans.*, 2016, **45**(38), 14954–14964.
13 L. Chen, Y. Tan, H. Xu, K. Wang, Z. H. Chen, N. Zheng, Y. Q. Li and L. R. Lin, *Dalton Trans.*, 2020, **49**(46), 16745–16761.
14 P. Halaš, I. Nemec and R. Herchel, *Magnetochemistry*, 2023, **9**(11), 229.
15 M. B. Hocking, *Can. J. Chem.*, 1969, **47**(24), 4567–4576.
16 M. L. Salum, C. J. Robles and R. Erra-Balsells, *Org. Lett.*, 2010, **12**(21), 4808–4811.
17 R. Boča and R. Herchel, *Program POLYMAGNET 2006–2021*.
18 P. Virtanen, R. Gommers, T. E. Oliphant, M. Haberland, T. Reddy, D. Cournapeau, E. Burovski, P. Peterson, W. Weckesser, J. Bright and S. J. Van Der Walt, *Nat. Methods*, 2020, **17**(3), 261–272.
19 C. Rajnák and R. Boča, *Coord. Chem. Rev.*, 2021, **436**, 213808.
20 S. Stoll and A. Schweiger, *J. Magn. Reson.*, 2006, **178**, 42–55.
21 A. V. Palii, D. V. Korchagin, E. A. Yureva, A. V. Akimov, E. Y. Misochko, G. V. Shilov, A. D. Talantsev, R. B. Morgunov, S. M. Aldoshin and B. S. Tsukerblat, *Inorg. Chem.*, 2016, **55**, 9696–9706.
22 S. Gómez-Coca, A. Urtizberea, E. Cremades, P. J. Alonso, A. Camón, E. Ruiz and F. Luis, *Nat. Commun.*, 2014, **5**, 4300.
23 F. Neese, F. Wennmohs, U. Becker and C. Riplinger, *J. Chem. Phys.*, 2020, **152**(22), 224108.
24 F. Neese, *Wiley Interdiscip. Rev.: Comput. Mol. Sci.*, 2022, **12**(5), e1606.
25 A. D. Becke, *Phys. Rev. A*, 1988, **38**(6), 3098.
26 F. Weigend and R. Ahlrichs, *Phys. Chem. Chem. Phys.*, 2005, **7**(18), 3297–3305.
27 F. Neese, *J. Comput. Chem.*, 2003, **24**(14), 1740–1747.
28 F. Weigend, *Phys. Chem. Chem. Phys.*, 2006, **8**(9), 1057–1065.
29 P. Å. Malmqvist and B. O. Roos, *Chem. Phys. Lett.*, 1989, **155**(2), 189–194.
30 C. Angeli, R. Cimiraglia, S. Evangelisti, T. Leininger and J. P. Malrieu, *J. Chem. Phys.*, 2001, **114**(23), 10252–10264.
31 C. Angeli, R. Cimiraglia and J. P. Malrieu, *Chem. Phys. Lett.*, 2001, **350**(3–4), 297–305.
32 A. Hellweg, C. Hättig, S. Höfener and W. Klopper, *Theor. Chem. Acc.*, 2007, **117**(4), 587–597.
33 F. Neese, F. Wennmohs, A. Hansen and U. Becker, *Chem. Phys.*, 2009, **356**(1–3), 98–109.
34 I. Nemec, R. Herchel, M. Kern, P. Neugebauer, J. Van Slageren and Z. Trávníček, *Materials*, 2017, **10**(3), 249.
35 F. Neese, *Wiley Interdiscip. Rev.: Comput. Mol. Sci.*, 2025, **15**, e70019.
36 T. Yanai, D. P. Tew and N. C. Handy, *Chem. Phys. Lett.*, 2004, **393**, 51–57.
37 E. Caldeweyher, S. Ehlert, A. Hansen, H. Neugebauer, S. Spicher, C. Bannwarth and S. Grimme, *J. Chem. Phys.*, 2019, **150**, 154122.
38 M. Garcia-Ratés and F. Neese, *J. Comput. Chem.*, 2020, **41**, 922.
39 V. Barone and M. Cossi, *J. Phys. Chem. A*, 1998, **102**, 1995.
40 Rigaku Oxford Diffraction, *CrysAlisPro 1.171.40.82a*, 2020.
41 G. M. Sheldrick, *Acta Crystallogr., Sect. A: Found. Adv.*, 2015, **71**, 3–8.
42 L. J. Bourhis, O. V. Dolomanov, R. J. Gildea, J. A. K. Howard and H. Puschmann, *Acta Crystallogr., Sect. A: Found. Adv.*, 2015, **71**, 59–75, DOI: 10.1107/S2053273314022207.
43 O. V. Dolomanov, L. J. Bourhis, R. J. Gildea, J. A. K. Howard and H. Puschmann, *J. Appl. Crystallogr.*, 2009, **42**, 339–341.